

Towards Wireless Ranging and Synchronization using CubeSat Software-Defined Radio Subsystems

Markus Gardill

Chair for Electronic Sensors and Systems
Brandenburg University of Technology
Cottbus, Germany
markus.gardill.de@ieee.org

Dominik Pearson

Center for Telematics
Würzburg, Germany
dominik.pearson@telematik-zentrum.de

Julian Scharnagl

Center for Telematics
Würzburg, Germany
julian.scharnagl@telematik-zentrum.de

Klaus Schilling

Center for Telematics
Würzburg, Germany
klaus.schilling@telematik-zentrum.de

An approach towards wireless ranging and synchronization using commercial off-the-shelf software-defined radio payloads for small satellites, esp. CubeSats is studied. The approach only relies on the programmable logic configuration and processing system software. No hardware modifications or additions to the payloads are necessary. Experimental evaluation of the initial implementation shows a standard deviation of time-of-flight-based ranging measurements in the order of 1 cm, which renders the concept of interest for distributed satellite system missions.

Index Terms—component, formatting, style, styling, insert

I. INTRODUCTION

Cooperating satellites allow for new application areas, improved mission performance and cost savings and thus receive increasing interest in recent years.

Several manifestations of this concept have been reported, ranging from distributed satellite systems (DSSs), e.g., for improved communications [1] or satellite formation flying (SFF) for Earth observation [2]–[4], up to the concept of Fractionated Spacecraft [5]. Depending on the mission requirements, precise synchronization and ranging are necessary between individual satellites, especially for missions with very high relative positioning or synchronization requirements that cannot be met by typical global navigation satellite system (GNSS) receivers for small satellites. A recent overview on synchronization for DSS is presented in [6].

While the DSS concept has been studied for several classes of satellites, it is of particular interest for small satellites, often implemented according to the CubeSat standard [7]. References [8], [9] indeed describe CubeSat-based DSS missions, but high-precision wireless synchronization as, e.g., used in large-scale missions such as [2], is typically not applied.

A method for wireless sub-nanosecond synchronization for terrestrial software-defined radio (SDR) networks has, e.g., recently been proposed in [10], achieving sub nanosecond synchronization for phase-coherent distributed systems. The authors achieve excellent results for multiple nodes, but rely on a pre-synchronization, e.g., using GNSSs. Based on the

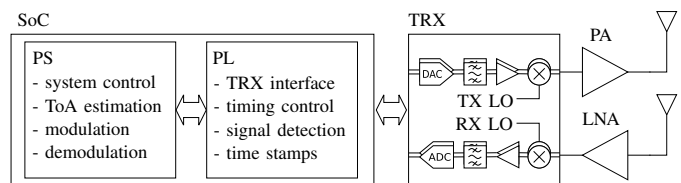


Fig. 1. Typical architecture of SDR for CubeSat applications. A fully integrated front-end is interfaced to a SoC including PL and PS resources. The mentioned bullet points indicate how wireless ranging and synchronization proposed in this work is realized by functions implemented in the PL and PS.

concept from [10], in this work we want to study how the method can be applied to commercial off-the-shelf (COTS) CubeSat SDR payloads, without requiring any additional pre-synchronization.

II. CUBESAT SOFTWARE-DEFINED RADIO ARCHITECTURE

SDRs are increasingly being used in CubeSats [7]. Their architecture often consists of an integrated transceiver (TRX) together with a System-on-a-Chip (SoC), i.e., a combination of field-programmable gate array (FPGA) programmable logic (PL) and a general-purpose processor-based processing system (PS), as illustrated in Fig. 1.

Specific realizations are, e.g., based on Analog Devices AD936x TRXs together with Xilinx Zynq-7000 family SoCs. Several COTS CubeSat SDRs are available implementing this architecture, e.g. refer to the products from [11], [12].

In this work, we consequently consider how precise ranging and synchronization can be implemented using this architecture, i.e., only as a software configuration option to be easily integrated in an SDR-equipped CubeSat mission.

III. TWO-WAY TIME TRANSFER

A general idea for synchronization is two-way time transfer (TWTT). It has a long heritage and has been reported in several works for satellite applications before [13]. We hence only present the main ideas and our models in this work, for a

more elaborate review the reader is e.g., referred to [10]. We consider a linear clock model according to

$$\tau_i = \alpha_i t + \phi_i, \quad (1)$$

where τ_i is the local clock of satellite $i \in \{A, B\}$, t is the global clock, α_i is the clock skew (frequency difference) and ϕ_i is the clock offset. It is assumed to be adequate for the relatively short synchronization intervals considered in this case study, although higher-order clock-models have been reported for improved accuracy [14].

Three parameters are of interest to solve the synchronization and ranging challenge: the time of flight (ToF) T_{ToF} , which is related to the distance $d_{A,B}$ between both satellites and the velocity of propagation c_0 by $T_{\text{ToF}} = d_{A,B}/c_0$, the time offset $\Delta T_{A,B} = \phi_B - \phi_A$ between both satellites, and the relative clock skew α_A/α_B . As illustrated in Fig. 2, the principle of TWTT is to estimate all those parameters by time-stamping the time instances of receive (RX) and transmit (TX) of synchronization waveforms exchanged between the satellites, collecting this timing information at a single node (e.g., transmitting $\tau_{B,RX}$ and $\tau_{B,TX}$ to satellite A), and solving a set of equations. If multiple TWTT measurements are used, we denote this by adding the index N to all quantities. If the focus is only on a single TWTT measurement, this index is dropped for convenience.

An initial estimate of the clock offset could be obtained by

$$\Delta \hat{T}'_{A,B} = \frac{(\tau_{B,RX} + \tau_{B,TX}) - (\tau_{A,RX} + \tau_{A,TX})}{2}. \quad (2)$$

However, by plugging the clock model from (1) in (2) it can be seen that $\Delta \hat{T}'_{A,B,N} = \Delta T_{A,B,N}$ only holds for identical clock-skews $\alpha_A = \alpha_B$. Else an error term prevails in (2). One solution if a non-zero clock-skew exists is to use two successive TWTT measurements, because from $\Delta \hat{T}'_{A,B,N+1} - \Delta \hat{T}'_{A,B,N}$ it can be shown that

$$\frac{\alpha_B}{\alpha_A} = \frac{2(\Delta \hat{T}'_{A,B,N+1} - \Delta \hat{T}'_{A,B,N})}{\tau_{A,TX,N+1} - \tau_{A,TX,N} + \tau_{A,RX,N+1} - \tau_{A,RX,N}} + 1. \quad (3)$$

Once (3) has been determined the ToF can be estimated by a single TWTT measurement using

$$\hat{T}_{\text{ToF}} = \frac{\tau_{A,RX} - \tau_{A,TX}}{2} - \frac{\alpha_B}{\alpha_A} \frac{\tau_{B,TX} - \tau_{B,RX}}{2}. \quad (4)$$

A corrected clock-offset estimate is then given by

$$\Delta \hat{T}_{A,B} = \frac{(\tau_{B,RX} + \tau_{B,TX})}{2} - \left(\tau_{A,TX} + \frac{\alpha_B}{\alpha_A} \frac{\tau_{A,RX} - \tau_{A,TX}}{2} \right). \quad (5)$$

Note that (5) is based on a transformation which sets $t_{A,RX,N} = 0$, i.e., the current TWTT measurement starts at zero global time. This is equivalent to $\tau_{A,RX,N} = \alpha_A t_{A,RX,N} + \phi_A = \phi_A$. Clearly, the framework of equations (3), (4), and (5) allows to solve the synchronization challenge by determining $\tau_{A,TX,n}$, $\tau_{B,RX,n}$, $\tau_{B,TX,n}$, $\tau_{A,RX,n}$ from two successive TWTT measurements $n \in N, N+1$.

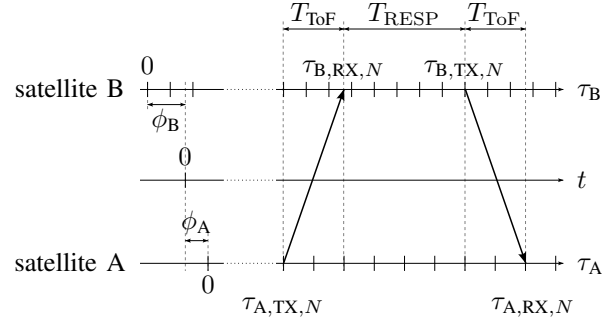


Fig. 2. Illustration of clock model and single TWTT measurement N .

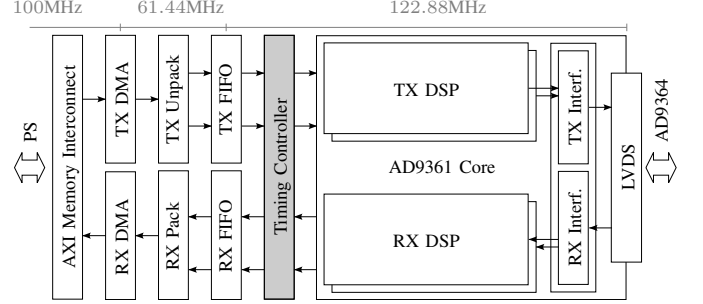


Fig. 3. HDL design of PL used in this work including clock domains. The Timing Controller implements the synchronization logic developed in this work, the remaining blocks are based on a publicly available reference design.

IV. LOGIC IMPLEMENTATION

For the basic implementation of an AD936x-based SDR together with a Zynq-based SoC, hardware description language (HDL) reference designs are available from Analog Devices [15]. However, the reference design basically performs TX and RX via buffers, which are filled and read by the PS. To obtain the required time-stamped measurements for TWTT, two additional mechanisms need to be implemented in the PL: the TX timing must be precisely controlled, such that $\tau_{i,TX,n}$, $i \in \{A, B\}$ are precisely known in the local time base and the RX time of arrival (ToA) must be estimated such that $\tau_{i,RX,n}$, $i \in \{A, B\}$ are determined. Therefore, the HDL reference design has been extended as illustrated in Fig. 3.

To achieve precisely controlled TX timing, the basic idea of our implementation is to fill the TX buffer as usual, but block the data path at some point until the desired TX time stamp $\tau_{i,TX,n}$, $i \in \{A, B\}$ is reached by the system's clock. To obtain the time stamps $\tau_{i,RX,n}$, $i \in \{A, B\}$ in the RX direction, the RX data stream is continuously monitored by the timing controller. Only if a signal is detected by the PL, the RX buffer is filled, a time stamp is added to the first sample of the RX buffer and the buffer is processed by the PS. Signal detection is currently based on a received signal strength indicator (RSSI) threshold, but more robust methods such as the use of correlation-based preamble detection could be easily implemented. Via this single timing reference in the RX buffer, the precise $\tau_{i,RX,n}$, $i \in \{A, B\}$ can be determined

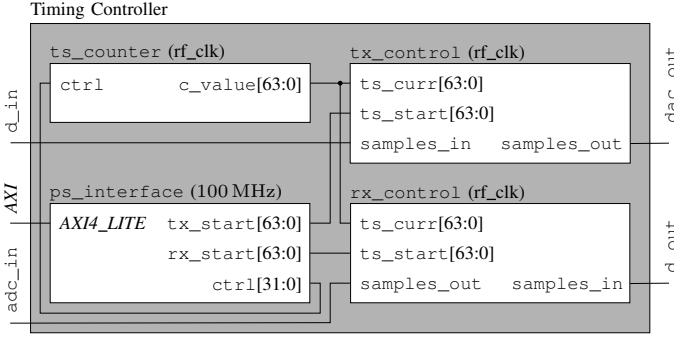


Fig. 4. Simplified structure of timing controller IP-core. While several additional details are hidden, note in particular that most blocks are clocked at the RF clock $f_{\text{rf_clk}} = 2 \cdot f_s$. The PS interface operates at 100 MHz and contains additional logic to ensure correct clock-domain crossing.

by a correlation-based approach in the PS, exploiting the characteristics of the synchronization waveforms.

The simplified HDL structure of the specific Timing Controller implementation is illustrated in Fig. 4. The `ps_interface` module implements the AXI4-LITE interface and is used to control the entire Timing Controller IP-Core. All parameters required to control the IP-Core can be set through register writes from the PS. Status bits from all the modules are collected in one register and can be read by the PS.

The `ts_counter` module provides the timing reference both for the `tx_control` and `rx_control` modules. It does so by counting the rising clock edges of the `rf_clk` clock and outputs this value in the 64 Bit signal `c_value`. The timing control of the transmit path is implemented by the `tx_control` module. It is achieved by interfering with the data interface between the FIFO buffers (`d_in`) and AXI9361 (`dac_out`). The current timer value provided by the `ts_counter` module is compared against the timestamp of the desired start of transmission. The signal of the comparator output feeds a multiplexer that either ties down the data path signals or connects the signals between the FIFO buffer directly to the signals of the AXI9361 core, without modifying them.

The `rx_control` module implements all features related to the timing control of the RX path. It supports two modes of operation. As illustrated in Fig. 4, it can either start a reception triggered by reaching a desired timestamp `tx_start`, just as the `tx_control` module does for transmissions. However, it also provides a mode of operation where receptions are triggered by exceeding a configurable signal power value. Therefore, the `rx_control` module includes logic to calculate the *RSSI* of the received signal in real time. In both modes, the timestamp `ts_start` of the first accepted sample is written to a register, which can be read by the PS.

V. SIGNAL PROCESSING

Like the method proposed in [10], chirp signals are used as synchronization waveforms. The equivalent complex baseband

(ECB) representation of the chirp signal $s(t)$ is given by

$$s(t) = \begin{cases} \exp\left(j2\pi\left(\frac{B_c f_s}{2l_c}t - \frac{B_c}{2}\right)t\right) & \text{for } 0 \leq t \leq T_c \\ 0 & \text{otherwise} \end{cases}, \quad (6)$$

where B_c is the bandwidth of the Chirp, f_s the sampling rate, l_c the length of the chirp in samples, and $T_c = l_c/f_s$ the duration of the chirp. Since the chirp is generated in the time domain τ_A of satellite A , the ECB signal $r_B(\tau_B)$ received by satellite B is subject to the time transformation $\tau_A \rightarrow \tau_B$. It then appears as

$$r_B(\tau_B) = s\left(\frac{\alpha_A}{\alpha_B}(\tau_B - \tau_{B,RX})\right) e^{j2\pi f_{\text{err}}\tau_B} e^{-j2\pi f_c(\alpha_B^{-1}\alpha_A(\phi_B + \tau_{B,\text{ToF}}) - \phi_A)} e^{\gamma_{A,B}^{\text{err}}}, \quad (7)$$

where f_{err} is the frequency and $\gamma_{A,B}^{\text{err}}$ the phase difference between both satellites, and $\tau_{B,\text{ToF}}$ is the ToF expressed in the clock domain of satellite B. To estimate the ToA, satellite B generates the chirp (6) in its own time base and performs the discrete-time equivalent of the correlation $d_{A,A}(\tau'_B) = (s \star r_B)(\tau'_B)$ with the received signal (τ'_B is used to denote the correlation lags). A peak detection followed by peak interpolation based on a sinc nonlinear least-squares is then used to estimate $\hat{\tau}_{B,RX} = \arg\max_{\tau'_B} |d_{A,B}(\tau'_B)|$ with sub-sample accuracy from the discrete-time correlation result.

Exchange of the timestamps between the stations is realized by a simple differential quadrature phase-shift keying (DQPSK) scheme implemented in the PS.

A complete baseband waveform $w(t)$ as used for the TWTT is shown in Fig. 5. The chirp signal has a bandwidth of $B_c = 38$ MHz, is sampled at $f_s = 61.44$ MHz and has a length of $l_c = 512$. The duration therefore is $T_c = l_c/f_s = 8.3$ μs , resulting in a sweep rate of $B_c/T_c = 4.56 \times 10^{12}$ Hz s^{-1} . The DQPSK part contains eight status bits, the TX timestamp ($\tau_{B,\text{TX}}$) encoded with 64 bits as well as the RX timestamp ($\tau_{B,\text{RX}}$) encoded with 128 bits. The waveform was recorded at node A during a TWTT measurement that was performed using antennas as described in section VI.

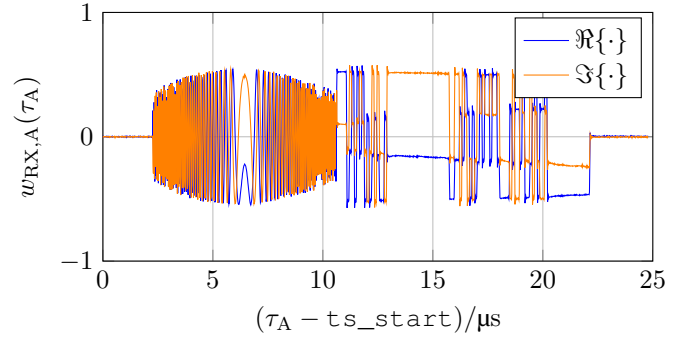


Fig. 5. Complete TWTT baseband waveform recorded at node A consisting of received chirp signal $r_A(\tau_A)$ and DQPSK-modulated timestamps. $\Re\{\cdot\}$ refers to the real part, $\Im\{\cdot\}$ to the imaginary part of the ECB signal.

VI. EXPERIMENTAL EVALUATION

The experimental evaluation was done using development kits based on an Avnet Zedboard with AD-FMCOMMS4-EBZ module, according to recommendations for the CubeSat SDR platform from [11]. Two of those evaluation kits were used in different configurations during the evaluation: a) connected by cables and b) by using 7 dBi antennas connected to the radio-frequency (RF) ports of the FMCOMMS4 modules at a device distance of about 1.8 m.

To study how the waveform parameters influence the precision of the ToF measurement, the variance σ_{ToF} of estimating T_{ToF} in the clock domain of system A was estimated using $n_{\text{trial}} = 1000$ TWTT measurements for different B_c and l_c . The results are presented in Fig. 6.

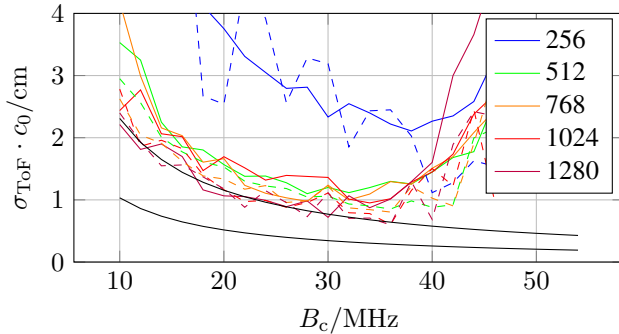


Fig. 6. Measured standard deviation for estimation of T_{ToF} using two experimental platforms vs. chirp bandwidth, evaluated for different chirp lengths. Dashed lines show cable-connected configuration, solid lines show wireless configuration. Solid black lines are CRLB for chirp lengths of 256 (upper line) and 1280 (lower line) evaluated at an SNR of 30 dB.

It can be seen that the measured results follow the trend modeled by the CRLB up to a bandwidth of about $B_c \approx 40$ MHz. The reason for the starting deviation at this frequency has not entirely been determined, but is attributed to a general degradation of the sinc nonlinear least-squares peak interpolation when B_c approaches the system sampling rate of $f_s = 61.44$ MHz, which was also observed in simulations. A precision (in terms of standard deviation) of around $\sigma_{\text{ToF}} \cdot c_0 \approx 1$ cm could be realized at a bandwidth of $B_c = 36$ MHz.

VII. CONCLUSION

We have shown in this work, that wireless synchronization and ranging can be achieved with state-of-the-art SDR payload architectures for small satellites and even CubeSats. The entire mechanism is implemented in the PL and PS of the system and does not require any external hardware or pre-synchronization. Since the current approach was evaluated in a lab setup, future work is focused on the integration of the experimental evaluation platform with external devices such as power amplifier (PA) and low-noise amplifier (LNA) for a realistic evaluation of the approach considering satellite distances of up to 100's of km.

REFERENCES

- [1] N. Saeed, A. Elzanaty, H. Almorad, H. Dahrouj, T. Y. Al-Naffouri, and M.-S. Alouini, "CubeSat communications: Recent advances and future challenges," *IEEE Communications Surveys & Tutorials*, vol. 22, no. 3, pp. 1839–1862, 2020.
- [2] M. Bachmann, T. Kraus, A. Bojarski, M. Schandri, J. Boer, T. Busche, J.-L. Bueso Bello, C. Grigorov, U. Steinbrecher, S. Buckreuss, G. Krieger, and M. Zink, "The TanDEM-X Mission Phases—Ten Years of Bistatic Acquisition and Formation Planning," *IEEE Journal of Selected Topics in Applied Earth Observations and Remote Sensing*, vol. 14, pp. 3504–3518, 2021.
- [3] K. Schilling, P. Bangert, S. Busch, S. Dombrovski, A. Freimann, A. Kramer, T. Nogueira, D. Ris, J. Scharnagl, T. Tzschichholz, G. Is-las, and L. Zhou, "Netsat: A Four Pico/Nano-Satellite Mission For Demonstration Of Autonomous Formation Flying," *th International Astronautical Congress*, p. 6, 2015.
- [4] L. Draschka, P. D. Kremmydas, A. Aumann, J. Scharnagl, K. Schilling, M. Tzabari, V. Holodovsky, Y. Schechner, O. Altaratz, and I. Koren, "Retrieving 3D microphysical properties of shallow clouds with nanosatellites flying in formation," in *Proceedings of the 72th International Astronautical Congress*. Dubai, UAE: IAF, 2021.
- [5] M. N. Sweeting, "Modern Small Satellites-Changing the Economics of Space," *Proceedings of the IEEE*, vol. 106, no. 3, pp. 343–361, Mar. 2018.
- [6] L. M. Marrero, J. C. Merlano-Duncan, J. Querol, S. Kumar, J. Krivochiza, S. K. Sharma, S. Chatzinotas, A. Camps, and B. Ottersten, "Architectures and Synchronization Techniques for Distributed Satellite Systems: A Survey," *IEEE Access*, vol. 10, pp. 45 375–45 409, 2022.
- [7] NASA, "State of the Art Small Spacecraft Technology (2020)," Nasa, Tech. Rep., 2020.
- [8] J. Scharnagl, R. Haber, V. Dombrovski, and K. Schilling, "Net-sat—challenges and lessons learned of a formation of 4 nano-satellites," *Acta Astronautica*, vol. 201, pp. 580–591, 2022. [Online]. Available: <https://www.sciencedirect.com/science/article/pii/S009457652200501X>
- [9] M. von Arnim, I. Mammadov, L. Draschka, J. Scharnagl, and K. Schilling, "THE CLOUDCT FORMATION OF 10 NANO-SATELLITES FOR COMPUTED TOMOGRAPHY TO IMPROVE CLIMATE PREDICTIONS," in *Proceedings of the 73th International Astronautical Congress*. Paris, France: IAF, 2022.
- [10] S. Prager, M. S. Haynes, and M. Moghaddam, "Wireless Subnanosecond RF Synchronization for Distributed Ultrawideband Software-Defined Radar Networks," *IEEE Transactions on Microwave Theory and Tech-niques*, pp. 1–1, 2020.
- [11] Alén Space, "Small Satellite Payloads," <https://alen.space/nanosatellite-payloads/>.
- [12] GOMSpace, "GOMSpace — Software Defined Radio," <https://gomspace.com/shop/subsystems/payloads/software-defined-radio.aspx>.
- [13] D. Kirchner, "Two-way time transfer via communication satellites," *Proceedings of the IEEE*, vol. 79, no. 7, pp. 983–990, Jul. 1991.
- [14] Y. Xie, G. J. M. Janssen, and A.-J. van der Veen, "A practical clock synchronization algorithm for UWB positioning systems," in *2016 IEEE International Conference on Acoustics, Speech and Signal Processing (ICASSP)*. Shanghai: IEEE, Mar. 2016, pp. 3891–3895.
- [15] Analog Devices, "HDL Reference Designs," <https://github.com/analogdevicesinc/hdl>, Sep. 2022.